On causality and aural impulse responses synthesized using the inverse discrete Fourier transform

Kren Monrad Nørgaard, Jont B. Allen, and Stephen T. Neely

Citation: The Journal of the Acoustical Society of America **149**, 3524 (2021); doi: 10.1121/10.0005048
View online: https://doi.org/10.1121/10.0005048
View Table of Contents: https://asa.scitation.org/toc/jas/149/5
Published by the Acoustical Society of America

JASA ARTICLE

On causality and aural impulse responses synthesized using the inverse discrete Fourier transform

Kren Monrad Nørgaard,[1,a)] Jont B. Allen,[2] and Stephen T. Neely[3]
[1]*Interacoustics A/S, Audiometer Allé 1, Middelfart DK-5500, Denmark*
[2]*Department of Electrical and Computer Engineering, University of Illinois, Urbana-Champaign, 306 North Wright Street, Champaign, Illinois 61820, USA*
[3]*Boys Town National Research Hospital, 555 North 30th Street, Omaha, Nebraska 68131, USA*

ABSTRACT:
Causality is a fundamental property of physical systems and dictates that a time impulse response characterizing any causal system must be one-sided. However, when synthesized using the inverse discrete Fourier transform (IDFT) of a corresponding band-limited numerical frequency transfer function, several papers have reported two-sided IDFT impulse responses of ear-canal reflectance and ear-probe source parameters. Judging from the literature on ear-canal reflectance, the significance and source of these seemingly non-physical negative-time components appear largely unclear. This paper summarizes and clarifies different sources of negative-time components through ideal and practical examples and illustrates the implications of constraining aural IDFT impulse responses to be one-sided. Two-sided IDFT impulse responses, derived from frequency-domain measurements of physical systems, normally occur due to the two-sided properties of the discrete Fourier transform. Still, reflectance IDFT impulse responses may serve a number of practical and diagnostic purposes. © *2021 Acoustical Society of America*.
https://doi.org/10.1121/10.0005048
(Received 20 November 2020; revised 27 April 2021; accepted 30 April 2021; published online 24 May 2021)
[Editor: Christopher Shera] Pages: 3524–3533

I. INTRODUCTION

A time impulse response describes the response of a given system to a unit-impulse stimulation. Physical systems are inherently causal, and the time impulse response characterizing any causal system must be one-sided. That is, any response from the system cannot occur before the stimulus. A derived logical rationale is that a two-sided time impulse response cannot provide the exact characterization of any physical system. Previous reports, the contents of which we summarize below, used the terms *causal*, *non-causal*, and *anti-causal* to describe properties of impulse responses. Because causality is a property of systems rather than signals, we reserve these terms for the system and instead apply the similar terms *one-sided*, *two-sided*, and *negative-time one-sided*, respectively, to describe properties of impulse responses. Thus, *one-sided* without further specification implies that the impulse response is confined to non-negative times.

The human ear is a non-linear physical system that is often characterized by its reflectance transfer function in the ear canal as a function of frequency. Ear-canal reflectance and derived quantities such as power absorbance provide a basis for diagnosing conductive middle-ear disorders (e.g., Piskorski *et al.*, 1999; Keefe *et al.*, 2000) and compensating for effects of the ear-canal acoustics on otoacoustic-emission measurements (e.g., Souza *et al.*, 2014; Charaziak and Shera, 2017). Ear-canal reflectance represents the proportion of sound reflected in the ear canal by the middle ear and is conventionally measured using an ear probe inserted into and sealed to the ear canal, enabled by a preliminary calibration to obtain the ear-probe Thévenin-equivalent source parameters (e.g., Allen, 1986; Keefe *et al.*, 1992; Voss and Allen, 1994). The conventional calibration procedure consists of measuring the pressure in several rigid acoustic waveguides and solving an over-determined system of equations at each frequency for the least-squares approximate source parameters (Allen, 1986). An alternative calibration method determines the ear-probe reflectance source parameters based on measurements in a semi-anechoic tube (e.g., Keefe, 1997; Keefe and Simmons, 2003).

Time impulse responses and frequency transfer functions are related through forward and inverse Fourier and one-sided Laplace transforms (Papoulis, 1962). Using the inverse discrete Fourier transform, several papers published in the Journal of the Acoustical Society of America (summarized in the following paragraph) have reported two-sided synthesized impulse responses of ear-canal reflectance as well as ear-probe source parameters. We denote synthesized inverse Fourier transform (IFT), inverse Laplace transform (ILT), and inverse discrete Fourier transform (IDFT) impulse responses as such to distinguish them from the general physical concept of a time impulse response. *Impulse response* without further specification refers to any of the impulse-response types described above.

a)Electronic mail: krng@interacoustics.com, ORCID: 0000-0002-6845-0388.

https://doi.org/10.1121/10.0005048

Voss and Allen (1994) observed negative-time components in the ear-canal-reflectance IDFT impulse response and explained that they occur due to fractional sample delays. After applying a low-pass frequency Blackman window to the transfer function that suppresses effects due to fractional sample delays, Rasetshwane and Neely (2011) still observed negative-time components in the reflectance IDFT impulse response, which they removed using time-reversed addition. Nørgaard *et al.* (2017a) found these components to arise due to evanescent modes and noted that they vanished when these modes were compensated. Similarly, Nørgaard *et al.* (2018) and Siegel *et al.* (2018) noted that the ear-probe source-parameter IDFT impulse responses are two-sided when evanescent modes are not accounted for during the calibration procedure. Based on previous studies on reflections between conical bores of different taper (Agulló *et al.*, 1988; Gilbert *et al.*, 1990; Agulló *et al.*, 1992; Agulló *et al.*, 1995), Nørgaard *et al.* (2019b) reported negative-time components in the ear-canal-reflectance IDFT impulse response when calculated from spherical-wave characteristic impedances. Most recently, Keefe (2020) incorporated a one-sided constraint to the ear-probe reflectance source-parameter IDFT impulse responses into the ear-probe calibration procedure. He proposed an increased measurement accuracy, explaining that negative-time components originate from the approximate least-squares solution to the over-determined system of equations, which does not retain one-sidedness. Keefe (2020) further proposed methods to measure reflectance time impulse responses that operate exclusively in the time domain, i.e., without the use of the IDFT. Robinson *et al.* (2013) used a zero-pole least-squares fitting procedure to obtain an approximate complex-analytic representation of the ear-canal reflectance and calculated the reflectance ILT impulse response, which is always one-sided.

Based on these reports, the significance and source of negative-time components in ear-canal and ear-probe IDFT impulse responses appear unresolved. Here, we aim to review and clarify various factors that contribute to negative-time components in IDFT impulse responses, explain their main causes, and explore the implications in practical ear-probe-calibration and reflectance-measurement scenarios. We further demonstrate the implications of constraining an IDFT impulse response to be one-sided and discuss the significance of such negative-time components.

II. BACKGROUND

A. Transfer functions and transforms

The forward Fourier $\mathcal{F}$ and one-sided Laplace $\mathcal{L}$ transforms relate real time impulse responses $h(t)$ as functions of time t to complex $H(\omega)$ and complex-analytic $H(s)$ transfer functions as functions of real angular frequency ω and complex Laplace frequency $s = \sigma + j\omega$ (Papoulis, 1962),

$$H(\omega) = \mathcal{F}[h(t)](\omega) \quad \text{and} \quad H(s) = \mathcal{L}[h(t)](s). \tag{1}$$

Given a continuous-time one-sided impulse response $h(t < 0) = 0$ and that both forward transforms converge, the time impulse response $h(t)$ can be recovered from either of the inverse transforms $\mathcal{F}^{-1}$ and $\mathcal{L}^{-1}$,

$$h(t) = \mathcal{F}^{-1}[H(\omega)](t) = \mathcal{L}^{-1}[H(s)](t). \tag{2}$$

The two transforms differ in a number of ways, in the context of our present objective most importantly in their constraints regarding one- and two-sided impulse responses (Papoulis, 1962; Allen, 2020). The forward one-sided Laplace transform integrates across the one-sided time axis $t \in [0, \infty)$, and the ILT impulse response is therefore always one-sided $h(t < 0) = 0$. The forward Fourier transform integrates across the two-sided time axis $t \in (-\infty, \infty)$, and the IFT therefore imposes no one-sided constraint onto the IFT impulse response. Additionally, the Fourier transform is only defined for bounded impulse responses, i.e., absolutely integrable (Papoulis, 1962), because the Fourier integral of a diverging time impulse response does not converge. The real part of the complex Laplace frequency σ allows the integral to converge and the one-sided Laplace transform of unbounded time impulse responses to exist within certain regions of convergence. However, the IFT of a transfer function that has an unbounded ILT impulse response does converge and results in a negative-time one-sided bounded IFT impulse response (e.g., Gilbert *et al.*, 1990).

In practice, measured acoustic transfer functions of physical systems $H(k)$ using transient stimuli are Hermitian-symmetric complex numerical functions of the real spectral bin number $k \in [[0, K-1]]$ (where double square brackets denote integer intervals) of a total of K frequency bins rather than complex-analytic functions of complex Laplace frequency s. Synthesizing IDFT impulse responses $h(n) = \text{IDFT}[H(k)]$ with the integer sample number $n \in [[-K/2, K/2-1]]$ therefore implicitly involves zero-phase frequency windowing $w(k) \in \mathbb{R}$. That is, negative-time components may be a result of time dispersion of the two-sided IDFT of such window $\text{IDFT}[w(k)]$. Calculating ILT impulse responses requires a complex-analytic transfer function (Robinson *et al.*, 2013; Allen, 2020).

B. Relations for one-sided time impulse responses

Papoulis (1962) summarized relations for one-sided impulse responses. Any impulse response $h(t)$ (whether one-sided or two-sided) can be decomposed into its even and odd components,

$$h_e(t) = \frac{h(t) + h(-t)}{2}, \tag{3}$$

$$h_o(t) = \frac{h(t) - h(-t)}{2}, \tag{4}$$

respectively, such that $h(t) = h_e(t) + h_o(t)$. Only if the impulse response is one-sided $h(t < 0) = 0$, then $h_e(t)$ and

$h_o(t)$ are directly related by $h(0)$ and the signum function $\mathrm{sgn}(t)$,

$$h_e(t) = h(0) + h_o(t)\,\mathrm{sgn}(t), \tag{5}$$

$$h_o(t) = h_e(t)\,\mathrm{sgn}(t). \tag{6}$$

Note that $h_e(t)$ and $h_o(t)$ are always two-sided. The one-sided time impulse response $\hat{h}(t)$ can now be recovered either from $h_e(t)$ or from $h_o(t)$ and $h(0)$,

$$\hat{h}(t) = 2\,\tilde{u}(t)\,h_e(t) = \tilde{u}(t)[h(t) + h(-t)] \tag{7}$$

$$= h(0) + 2\,\tilde{u}(t)\,h_o(t) = h(0) + \tilde{u}(t)[h(t) - h(-t)], \tag{8}$$

where $\tilde{u}(t) = [1 + \mathrm{sgn}(t)]/2$ is the Fourier step function with the half-maximum convention $\tilde{u}(0) = 1/2$ (Allen, 2020). Note that $\tilde{u}(t)$ is different from the Heaviside step function $u(t)$, which is undefined at $t = 0$. The hat signifies that $\hat{h}(t) \neq h(t)$ if the impulse response is not one-sided $h(t < 0) \neq 0$. Note that Eqs. (7) and (8) yield different $\hat{h}(t)$ when the time impulse response is not one-sided because $h(-t) \neq -h(-t)$.

C. Kramers–Kronig relations

The above time relations for one-sided time impulse responses $h(t < 0) = 0$ can be extended to the transfer function using the Fourier transform $H(\omega) = \mathcal{F}[h(t)](\omega)$, whose real Re and imaginary Im parts are given from $h_e(t)$ and $h_o(t)$, respectively (Papoulis, 1962),

$$\mathrm{Re}H(\omega) = \mathcal{F}[h_e(t)](\omega), \tag{9}$$

$$j\mathrm{Im}H(\omega) = \mathcal{F}[h_o(t)](\omega). \tag{10}$$

The Kramers–Kronig relations are frequency-domain equivalents of Eqs. (5) and (6), and based on the Hilbert transform $\mathcal{H}$ and $h(0) = H(\infty) \equiv \lim_{\omega\to\infty} H(\omega) \in \mathbb{R}$ [note that $h(t) \to 0$ for $t \to \infty$ only if $\mathrm{Im}H(\infty) = 0$] (Papoulis, 1962),

$$\mathrm{Re}H(\omega) = H(\infty) + \mathcal{H}[\mathrm{Im}H(\omega)], \tag{11}$$

$$\mathrm{Im}H(\omega) = \mathcal{H}^{-1}[\mathrm{Re}H(\omega)], \tag{12}$$

respectively. Similarly, recovering the transfer function $\hat{H}(\omega)$ with one-sided IFT impulse response $\hat{h}(t < 0) = \mathcal{F}^{-1}[\hat{H}(\omega)](t < 0) = 0$,

$$\hat{H}(\omega) = \mathrm{Re}H(\omega) + j\mathcal{H}^{-1}[\mathrm{Re}H(\omega)] \tag{13}$$

$$= H(\infty) + \mathcal{H}[\mathrm{Im}H(\omega)] + j\mathrm{Im}H(\omega). \tag{14}$$

The above time [Eqs. (5)–(8)] and frequency [Eqs. (11)–(14)] formulations are directly related through the Fourier transform, i.e., $\hat{H}(\omega) = \mathcal{F}[\hat{h}(t)](\omega)$, regardless of the impulse response not being one-sided $h(t < 0) \neq 0$. For continuous-time analysis, as with the Fourier transform, the Kramers–Kronig relations [Eqs. (11) and (12)] theoretically require integrating $H(\omega)$ up to infinite frequency.

D. Discrete-time relations

For practical discrete-time measurements with a finite number of frequency bins K, the time and frequency formulations are related through the discrete Fourier transform. Further, the Kramers–Kronig relations apply for the discrete Hilbert transform (DHT) (Gold *et al.*, 1969), for which the numerical implementation involves inverse and forward discrete Fourier transforms. The explicit discrete-time equivalents of Eqs. (7) and (8) are

$$\hat{h}(n) = 2\,\tilde{u}(n)\,h_e(n) = \tilde{u}(n)[h(n) + h(-n)] \tag{15}$$

$$= h(0) + 2\,\tilde{u}(n)\,h_o(n) = h(0) + \tilde{u}(n)[h(n) - h(-n)], \tag{16}$$

and similarly those for Eqs. (13) and (14) are

$$\hat{H}(k) = \mathrm{Re}H(k) + j\mathrm{IDHT}[\mathrm{Re}H(k)] \tag{17}$$

$$= h(0) + \mathrm{DHT}[\mathrm{Im}H(k)] + j\mathrm{Im}H(k), \tag{18}$$

where IDHT is the inverse discrete Hilbert transform (Gold *et al.*, 1969). The time and frequency relations then apply when the IDFT impulse response satisfies the periodic one-sided condition $h(n < 0) = 0$ (Oppenheim and Schafer, 1989). Thus, the practical utility of these relations is constrained by the properties of the discrete Fourier transform. Equation (15) is the one-sided constraint employed by Keefe (2020) and is effectively a time-reversed addition.

III. IDEALIZED EXAMPLES

A. Frequency windowing

Consider the τ-time delay transfer function

$$H(s) = e^{-s\tau}. \tag{19}$$

For $\tau \geq 0$, the transfer function $H(s)$ has identical inverse Fourier and Laplace transforms, which result in the one-sided IFT and ILT impulse response

$$h(t) = \mathcal{F}^{-1}[e^{-j\omega\tau}](t) = \mathcal{L}^{-1}[e^{-s\tau}](t) = \delta(t - \tau), \tag{20}$$

where $\delta(t)$ is the Dirac-delta function.

For discrete-time analysis, a corresponding numerical Hermitian-symmetric N-sample delay transfer function can be calculated as

$$H(k) = \begin{cases} e^{-j2\pi Nk/K}, & \text{for } k \in [[0, K/2 - 1]], \\ e^{j2\pi N(K-k)/K}, & \text{for } k \in [[K/2, K - 1]]. \end{cases} \tag{21}$$

Its IDFT impulse response can now be written as an infinite sum and a special case of an integer sample delay $N \in \mathbb{Z}$,

$$h(n) = \mathrm{IDFT}[H(k)w(k)]$$

$$= \sum_{m=-\infty}^{\infty} \mathrm{sinc}(n - N - mK) \overset{N\in\mathbb{Z}}{\Longrightarrow} \delta_{n,N}, \tag{22}$$

https://doi.org/10.1121/10.0005048

where $\delta_{n,N}$ is the Kronecker delta. The infinite summation of sinc functions $\mathrm{sinc}(n) = \sin(\pi n)/(\pi n)$ is a result of implicitly limiting the bandwidth of the transfer function using a rectangular window $w(k) = 1$ (Oppenheim and Schafer, 1989) and referred to as the Gibbs phenomenon. When K is adequately large, contributions from the sinc functions with $m \neq 0$ in the summation are negligible.

Panel columns of Fig. 1 show the magnitude and real and imaginary parts of the numerical transfer functions $H(k)$ [Eq. (21)], their IDFT impulse responses $h(n)$ [Eq. (22)], the magnitude and real and imaginary parts of the one-sided constrained transfer functions $\hat{H}(k)$ [Eq. (17)], and the IDFT impulse responses $\hat{h}(n)$ [Eq. (15)] for $K = 2048$ samples, with different sample delays N and frequency windows $w(k)$.

Figures 1(a)–1(d) show the case for the delay $N = 4$ samples (this delay resembles the round trip length of ear canals and rigid calibration waveguides at the audio sampling rate) and the rectangular window $w(k) = 1$. Because N is an integer and the phase $\angle H(K/2) = N\pi$, the spectrum for $k \geq K/2$ and the harmonic spectra are perfectly represented by Eq. (19). The two-sided sinc function $\mathrm{sinc}(n)$ is therefore sampled at integer $n \in \mathbb{Z}$, and $h(n)$ is one-sided. Consequently, the transfer function $\hat{H}(k)$ and impulse response $\hat{h}(n)$ can be exactly reconstructed from Eqs. (15) or (16) and Eqs. (17) or (18), respectively, using discrete Fourier and Hilbert transforms.

Figures 1(e)–1(h) show the case for the delay $N = 3.5$ samples and the rectangular window $w(k) = 1$, which result in an abrupt discontinuity at $k = K/2$ in the Hermitian-symmetric spectrum. The sinc function $\mathrm{sinc}(n)$ is now sampled at half-integers $n \in \mathbb{Z} + 1/2$, and $h(n)$ is two-sided (Voss and Allen, 1994). Applying a one-sided constraint to the transfer function $\hat{H}(k)$ and IDFT impulse response $\hat{h}(n)$ using Eqs. (15) and (17) still results in a one-sided $\hat{h}(n)$, but $\hat{H}(k)$ and $\hat{h}(n \geq 0)$ clearly differ from $H(k)$ and $h(n \geq 0)$, respectively, because they have been altered to suppress the negative-time components in $h(n)$ caused by the sinc function. In this case, the one-sided constraint effectively results in a low-pass filtration of the original transfer function $H(k)$, but the error in the reconstructed transfer function $\hat{H}(k)$ depends on the specific characteristics of $H(k)$. Note that, due to the way MATLAB draws figures by linearly interpolating between adjacent samples, $\hat{h}(n)$ may immediately appear two-sided because $\hat{h}(0) \neq 0$, but it is one-sided.

Finally, Figs. 1(i)–1(l) show the case for the delay $N = 3.5$ samples with the transfer function low-pass filtered by a Blackman window $w(k)$ (Rasetshwane and Neely, 2011). It is evident how the filtering causes a confined smearing of $h(n)$, and $\hat{H}(k)$ and $\hat{h}(n)$ can now be reconstructed with good accuracy despite the half-integer delay because the IDFT of a Blackman window is more localized in time than a sinc function. For delays N short enough that $h(n)$ extends below $t = 0$ into negative time, this results in notable changes to $\hat{H}(k)$ and $\hat{h}(n)$.

B. Unbounded impulse responses

Consider the transfer function $H(s)$ with a pole in the right-hand plane at $s = 1$,

$$H(s) = \frac{1}{1 - s}. \tag{23}$$

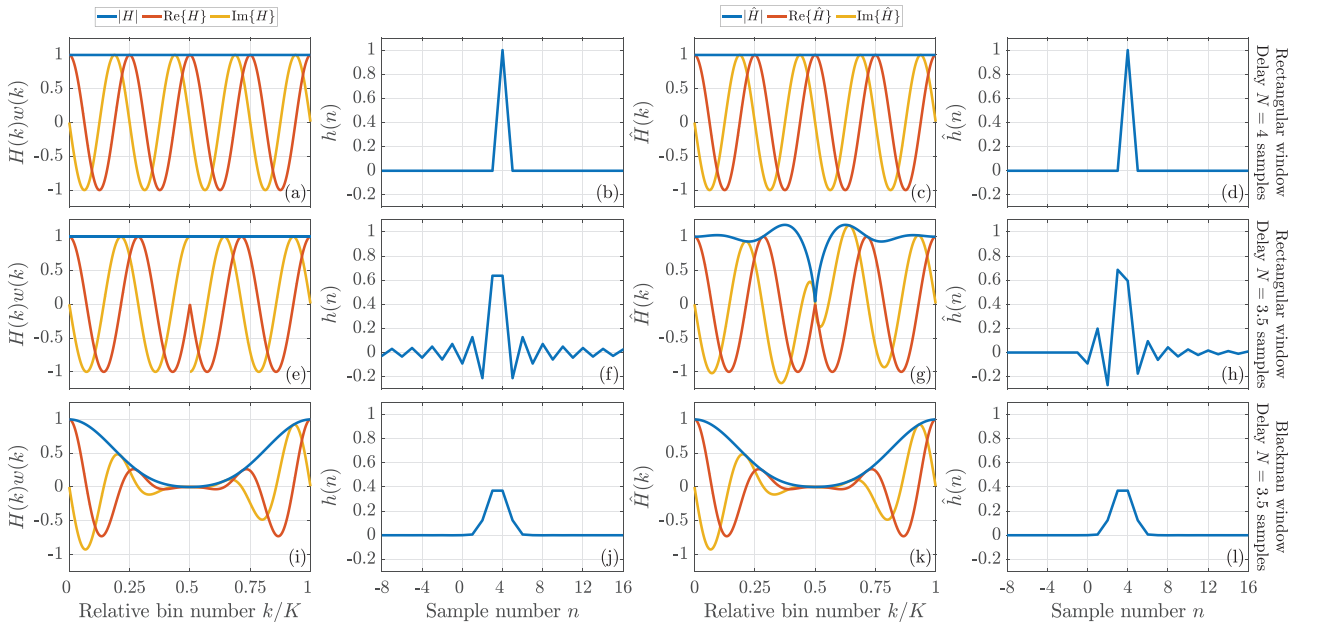

FIG. 1. (Color online) [(a), (e), and (i)] The magnitude and real and imaginary parts of the Hermitian-symmetric numerical transfer function $H(k)$ [Eq. (21)] as a function of the integer spectral bin number k of K total bins, multiplied by the frequency window $w(k)$, [(b), (f), and (j)] its IDFT impulse response $h(n)$ as a function of the integer sample number n and the one-sided constrained [(c), (g), and (k)] transfer functions $\hat{H}(k)$ [Eq. (17)] with [(d), (h), and (l)] impulse responses $\hat{h}(n)$ [Eq. (15)] for delays of [(a)–(d)] $N = 4$ samples and $w(k) = 1$, [(e)–(h)] $N = 3.5$ samples and $w(k) = 1$, and [(i)–(l)] $N = 3.5$ samples and a Blackman window $w(k)$ (Rasetshwane and Neely, 2011).

The transfer function has the ILT impulse response

$$h(t) = \mathcal{L}^{-1}\left[\frac{1}{1-s}\right](t) = -e^t u(t), \tag{24}$$

which is one-sided but is unbounded because $e^t \to \infty$ as $t \to \infty$. Despite the fact that the Fourier transform of the ILT impulse response $\mathcal{F}[-e^t u(t)](\omega)$ does not converge, the IFT of the transfer function [Eq. (23)] does converge and results in the IFT impulse response

$$h(t) = \mathcal{F}^{-1}\left[\frac{1}{1-j\omega}\right](t) = e^t\,\tilde{u}(-t), \tag{25}$$

which is a negative-time one-sided bounded function. Consequently, depending on the inverse transform used, the transfer function may characterize both a causal unstable system [Eq. (24)] and a non-causal stable system [Eq. (25)] (Allen, 2020).

Applying a one-sided constraint [Eq. (7)] to the IFT impulse response $h(t)$ of the transfer function with a right-hand-plane pole [Eq. (23)] results in time reversal,

$$\hat{h}(t) = h(-t) = e^{-t}\tilde{u}(t). \tag{26}$$

Accordingly, the transfer-function one-sided constraint using the corresponding Kramers–Kronig relation [Eq. (13)] results in complex conjugation (denoted by the asterisk superscript),

$$\hat{H}(\omega) = H^*(\omega) = \frac{1}{1+j\omega}. \tag{27}$$

One-sided constrained impulse responses and transfer functions using Eq. (8) or (14) result in opposite signs of operation in Eqs. (26) and (27). Constraining transfer functions with right-hand-plane poles to be one-sided does not remove the potentially problematic instability but rather mirrors its negative-time one-sided behavior resulting from the IFT into positive time. For numerical transfer functions and discrete Fourier transforms, these expressions are additionally subject to two-sided effects of windowing as discussed in Sec. III A.

IV. PRACTICAL EXAMPLES

This section describes practical examples in which different types of two-sided IDFT impulse responses occur. The considered examples include analytical representative ear-canal reflectances, measured reflectances in an occluded-ear simulator, and ear-probe calibrations. In all these cases, the influence of employing the one-sided constraint [Eqs. (15) and (17)] is explored.

A. Frequency windowing and reflectance

Fractional sample delays occur in ear canals to varying degrees with varying ear-canal lengths. We exemplify the practical implications of frequency windowing and fractional sample delays in an acoustic load similar to the human ear canal by modeling the ear-canal reflectance $R_{ec}(k)$ as a lossless delayed reflection from a representative tympanic-membrane impedance $Z_{tm}(k)$,

$$R_{ec}(k) = \frac{Z_{tm}(k) - Z_0}{Z_{tm}(k) + Z_0}\, e^{-j4\pi l_{ec} f_s k/(Kc)}. \tag{28}$$

The complex tympanic-membrane impedance $Z_{tm}(k)$ was modeled according to Nørgaard *et al.* (2019b) using two parallel acoustic RLC circuits to match the reflectance characteristic of a standardized occluded-ear simulator (IEC 60318–4, 2010) with a cross-sectional area $A_{ec} = 44.18$ mm^2. Furthermore, $Z_0 = \rho c/A_{ec}$ is the ear-canal characteristic impedance with air density ρ and speed of sound c, l_{ec} is the ear-canal length, and f_s is the sampling rate. Thus, the ear-canal reflectance of Eq. (28) characterizes an ideal causal stable acoustic system with a one-sided time impulse response similar to the adult ear canal.

Panel columns of Fig. 2 show modeled ear-canal reflectances $R_{ec}(k)$ [Eq. (28)] with l_{ec} ranging from 1.5 to 4 cm in 0.5-cm increments, the corresponding reflectance IDFT impulse responses $r_{ec}(n)$, and the one-sided constrained ear-canal reflectances $\hat{R}_{ec}(k)$ [Eq. (17)] with one-sided reflectance IDFT impulse responses $\hat{r}_{ec}(n)$ [Eq. (15)], with different frequency windows $w(k)$ and frequency-truncation approaches.

Figures 2(a)–2(d) show quantities using a rectangular frequency window $w(k) = 1$ and truncating the frequency spectrum at 20 kHz. This results in negative-time components due to fractional sample delays occurring randomly to varying degrees, depending on the delay of the main reflection from the tympanic membrane. Consequently, reconstructing the reflectances $\hat{R}_{ec}(k)$ to have one-sided reflectance IDFT impulse responses $\hat{r}_{ec}(n)$ results in errors similar to those in Fig. 1, depending on the ear-canal length.

Figures 2(e)–2(h) show quantities using a Blackman window $w(k)$ (Rasetshwane and Neely, 2011), similarly truncating the spectrum at 20 kHz, which effectively suppresses negative-time components due to fractional sample delays in the reflectance IDFT impulse responses $r_{ec}(n)$. It is evident that reflectances $\hat{R}_{ec}(k)$ can now be accurately reconstructed across most of the frequency spectrum to have one-sided IDFT impulse responses $\hat{r}_{ec}(n)$. In this case, there is of course little need to compute the one-sided constrained IDFT reflectance impulse responses because they were one-sided in the first place.

Finally, Figs. 2(i)–2(l) show quantities using a rectangular window $w(k) = 1$ and a frequency-truncation approach at the largest-possible frequencies where the reflectance phases $\angle R_{ec}(k)$ are integer multiples of π (Nørgaard *et al.*, 2017a), which suppresses negative-time components due to the sinc function in $r_{ec}(n)$. Similarly, reflectances $\hat{R}_{ec}(k)$ can now be accurately reconstructed to have a one-sided reflectance IDFT impulse response $\hat{r}_{ec}(n)$, although part of the spectrum is discarded in the truncation process.

B. Evanescent modes and reflectance

Considerations regarding windowing similar to those described in Secs. III A and IV A apply for other transfer

https://doi.org/10.1121/10.0005048

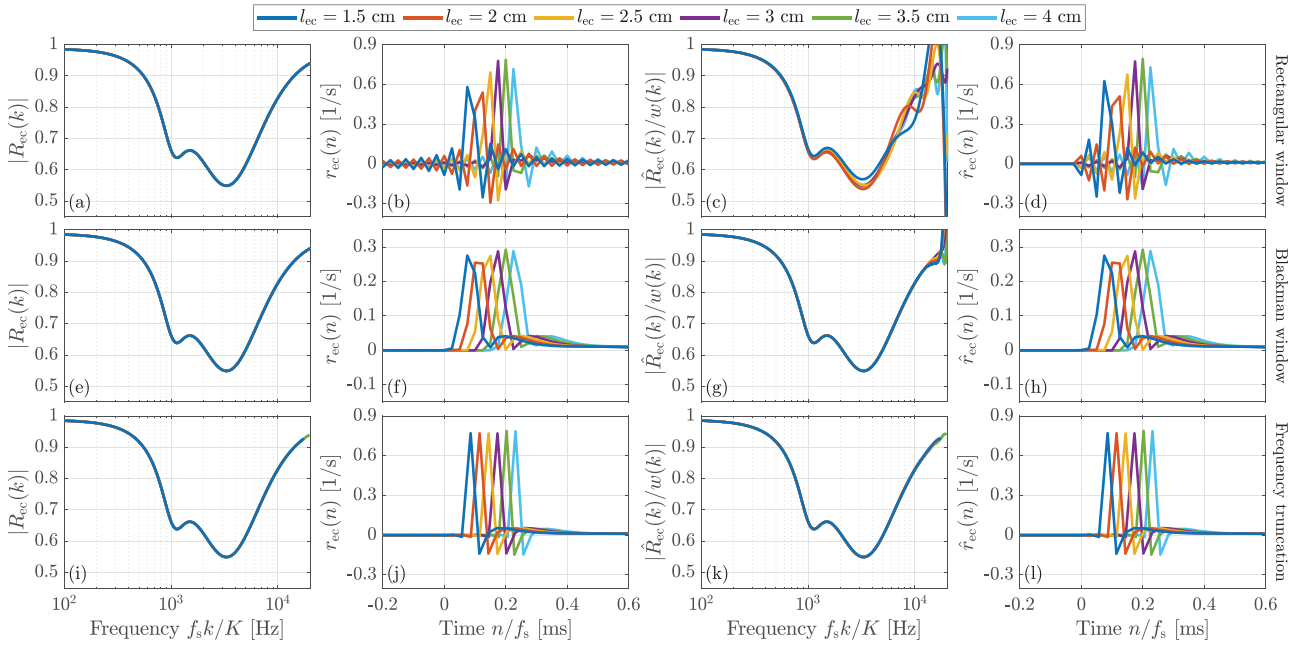

FIG. 2. (Color online) [(a), (e), and (i)] The ear-canal reflectances $R_{ec}(k)$ [Eq. (28)] with different ear-canal lengths calculated using causal transmission-line theory, [(b), (f), and (j)] the reflectance IDFT impulse responses $r_{ec}(n)$, and [(c), (g), and (k)] the reconstructed reflectances $\hat{R}_{ec}(k)$ [Eq. (17)] with [(d), (h), and (l)] one-sided reflectance IDFT impulse responses $\hat{r}_{ec}(n)$ [Eq. (15)]. Numerical results are shown using [(a)–(d)] a rectangular window $w(k) = 1$ and [(e)–(h)] a Blackman window $w(k)$ (Rasetshwane and Neely, 2011) truncating the frequency spectrum at 20 kHz, and [(i)–(l)] a rectangular window $w(k) = 1$ truncating the frequency spectrum according to Nørgaard *et al.* (2017a). Note that the shown ear-canal reflectances $R_{ec}(k)$ in (a), (e), and (i) are not multiplied by the corresponding frequency windows $w(k)$, and the reconstructed reflectances $\hat{R}_{ec}(k)$ in (c), (g), and (h) are divided by the frequency windows $w(k)$ to restore the actual frequency content.

functions, e.g., the impedance $j\omega L$ of an inertance L, which approximates the series impedance of higher-order evanescent modes (Karal, 1953; Keefe and Benade, 1981). The IDFT impulse response of such inertance is sampled using the sinc-function derivative $\mathrm{sinc}'(n) = \cos(\pi n)/n - \sin(\pi n)/(\pi n^2)$ at integer $n \in \mathbb{Z}$ (Nørgaard *et al.*, 2018). Using the inverse Fourier or Laplace transform, the impedance IFT or ILT impulse response of the inertance $h(t) = \mathcal{F}^{-1}[j\omega L] = \mathcal{L}^{-1}[sL] = L\delta'(t)$, with the Dirac-delta derivative $\delta'(t)$. While an inertance is a causal component, its impedance IDFT impulse response is a two-sided odd function.

Figure 3 shows quantities and conditions identical to Fig. 2 of ear-canal reflectance measurements in a uniform standardized occluded-ear simulator (IEC 60318-4, 2010). The measurements were adopted from Fig. 5(c) of Nørgaard *et al.* (2019a), using a perpendicular ear-probe insertion with different ear-canal lengths l_{ec} and a fixed characteristic impedance Z_0 corresponding to a cross-sectional area $A_{ec} = 44.18\ \mathrm{mm}^2$. That is, the measurements represent an ideal laboratory setting, affected only by evanescent modes and frequency windowing. Note that the manual ear-probe insertion results in some uncertainty in the ear-canal length. Evanescent modes introduce a dependency of the reflectances $R_{ec}(k)$ on insertion depth, and negative-time components in the reflectance IDFT impulse responses $r_{ec}(n)$ due to evanescent modes are clearly visible for all windowing and truncation approaches. It is interesting that the influence of evanescent modes is largely remedied in the one-sided constrained reflectances $\hat{R}_{ec}(k)$, which vary less with ear-canal length. This is because the effect of evanescent modes on the reflectance IDFT impulse response $r_{ec}(n)$ is a superimposed partly odd function, and Eq. (15) reconstructs $\hat{r}_{ec}(n)$ from the even part of $r_{ec}(n)$. Notice also how the two-sided effects due to fractional sample delays are reduced compared to the modeled results of Fig. 2. The measured ear-canal reflectances in Fig. 3 are nearly identical to the modeled reflectances of Fig. 2 up to 10 kHz; however, the occluded-ear simulator has a protection grid and dust protector mounted near its reference input plane. This results in a decreased reflectance beyond 10 kHz and effectively a low-frequency filtration.

C. Unstable components and constrained calibrations

Unbounded acoustic ILT impulse responses as described in Sec. III B result from non-physical systems, e.g., an anechoic contracting conical horn; reflections will occur at the apex of such a horn (Chapman, 1989; Gilbert *et al.*, 1990; Agulló *et al.*, 1995). The transfer function in Eq. (23) has a form identical to the parallel negative inertance of the spherical-wave characteristic impedance looking toward the apex of the conical horn (Benade, 1988). The form is also identical to the negative parallel compliance observed in the ear-probe source-parameter IDFT impulse responses when evanescent modes are not accounted for during calibration (Nørgaard *et al.*, 2018; Siegel *et al.*, 2018). The hypothetical negative acoustic compliance is a

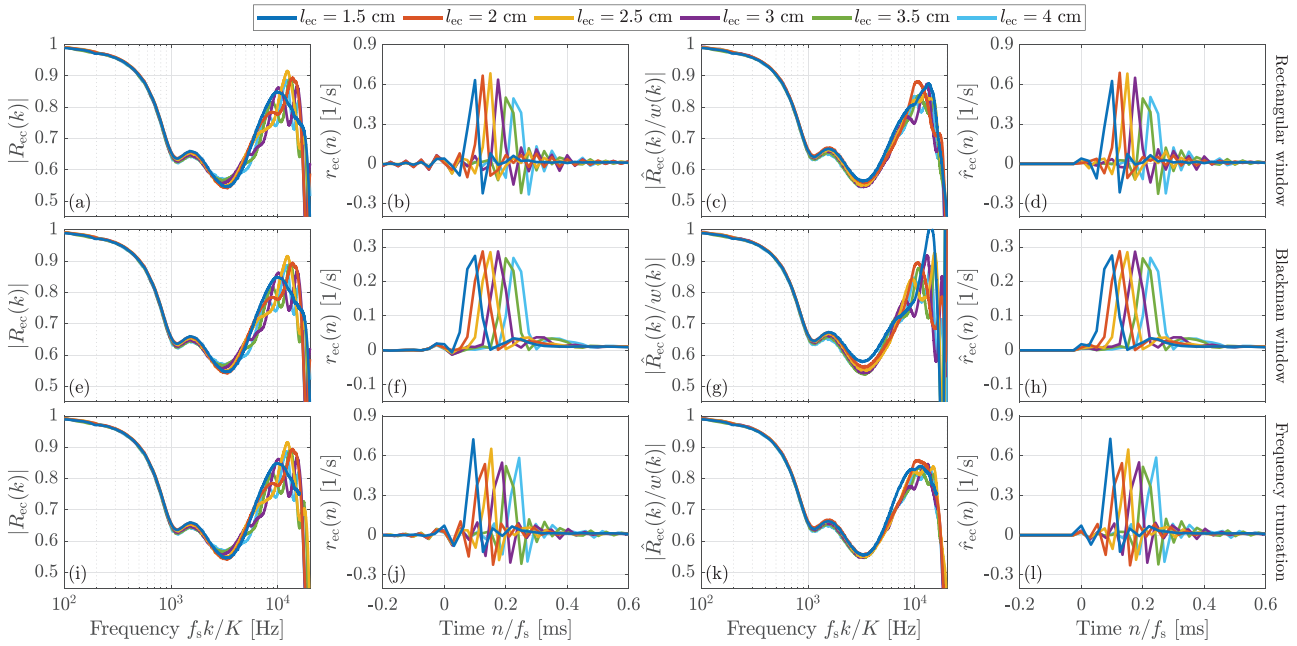

FIG. 3. (Color online) Quantities and conditions identical to Fig. 2 but showing measurements adopted from Fig. 5(c) of Nørgaard *et al.* (2019a), using perpendicular ear-probe insertions into the uniform occluded-ear simulator.

non-physical unstable but causal component (that is, a discharging acoustic volume flow from the compliance results in an increase in pressure). However, the IDFT impulse responses of such systems are negative-time one-sided due to the Fourier transform.

Here, we illustrate the implications of non-physical unstable components in ear-probe source parameters and constraining the ear-probe source-parameter IDFT impulse responses to be one-sided (Keefe, 2020). Results are shown for calibrations of the same ear probe, obtained as described and reported in Fig. 5 of Nørgaard *et al.* (2017b). That is, the two following unconstrained calibrations are obtained using sets of waveguides with

(1) 4-mm diameters and accounting for evanescent modes according to Nørgaard *et al.* (2017b) and
(2) 8-mm diameters and the conventional method of acoustically estimating waveguide lengths (e.g., Allen, 1986; Scheperle *et al.*, 2008), thus not accounting for evanescent modes.

Calibration (2) now contains a negative parallel compliance as a result of not accounting for evanescent modes (Nørgaard *et al.*, 2017b; Nørgaard *et al.*, 2018; Siegel *et al.*, 2018). For calibrations (1) and (2), a one-sided constrained calibration was calculated by applying the one-sided constraint according to Keefe (2020) [Eqs. (15) and (17)] to the ear-probe source impedance $Z_s(k)$, admittance $Y_s(k) = 1/Z_s(k)$, and reflectance $R_s(k) = [Z_s(k) - Z_0]/[Z_s(k) + Z_0]$, where Z_0 is the characteristic impedance of the occluded-ear simulator, resulting in a total of four calibrations. The one-sided constraint was not applied to the ear-probe source pressure $P_s(k)$ and incident pressure $P_0(k) = P_s Z_s(k)/[Z_0 + Z_s(k)]$, as described by Keefe (2020), because it had no qualitative impact on the results. Note that Keefe (2020) reformulated the least-squares solution to approximate only the real part of the source reflectance $\mathrm{Re}R_s(k)$ [opposed to the formulation of Allen (1986), which is used here], based on which the complex source reflectance $R_s(k)$ was reconstructed from Eq. (15) or (17), but the implications of the reconstruction are similar. For each type of ear-probe source parameters, the reflectances $R_{ec}^{Z_s}(k)$, $R_{ec}^{Y_s}(k)$, and $R_{ec}^{R_s}(k)$ of the occluded-ear simulator were measured using an approximate ear-canal length of 2.5 cm.

For all four calibrations, Figs. 4(a), 4(e), and 4(i) show the magnitudes and Figs. 4(b), 4(f), and 4(j) show the phases of the ear-probe source impedances $Z_s(k)$, admittances $Y_s(k)$, and reflectances $R_s(k)$; Figs. 4(c), 4(g), and 4(k) show their respective source-parameter IDFT impulse responses $z_s(n)$, $y_s(n)$, and $r_s(n)$; and Figs. 4(d), 4(h), and 4(l) show the ear-canal reflectances $R_{ec}^{Z_s}(k)$, $R_{ec}^{Y_s}(k)$, and $R_{ec}^{R_s}(k)$. Note that the ear-canal reflectances measured using the unconstrained calibrations (1) and (2) are similar because the combination of the parallel compliance and the inertance of evanescent modes constitutes a lumped-element extension of the transmission line (Nørgaard *et al.*, 2017b).

For the results based on the source impedance $Z_s(k)$ in Figs. 4(a)–4(d), the unstable negative parallel compliance is evident in Figs. 4(a) and 4(b) from the approximate $1/k$ behavior in $|Z_s(k)|$ and $\angle Z_s(k) \to 90°$ with increasing frequency for the unconstrained calibration (2) as opposed to the unconstrained calibration (1). Further, for the unconstrained calibration (2), the negative-time exponential decay resulting from the IDFT of the unstable negative parallel compliance [see Eq. (25)] is evident from $z_s(n)$ in Fig. 4(c), as opposed to the unconstrained calibration (1) for which $z_s(n)$ is close to being one-sided. The impulse response of

https://doi.org/10.1121/10.0005048

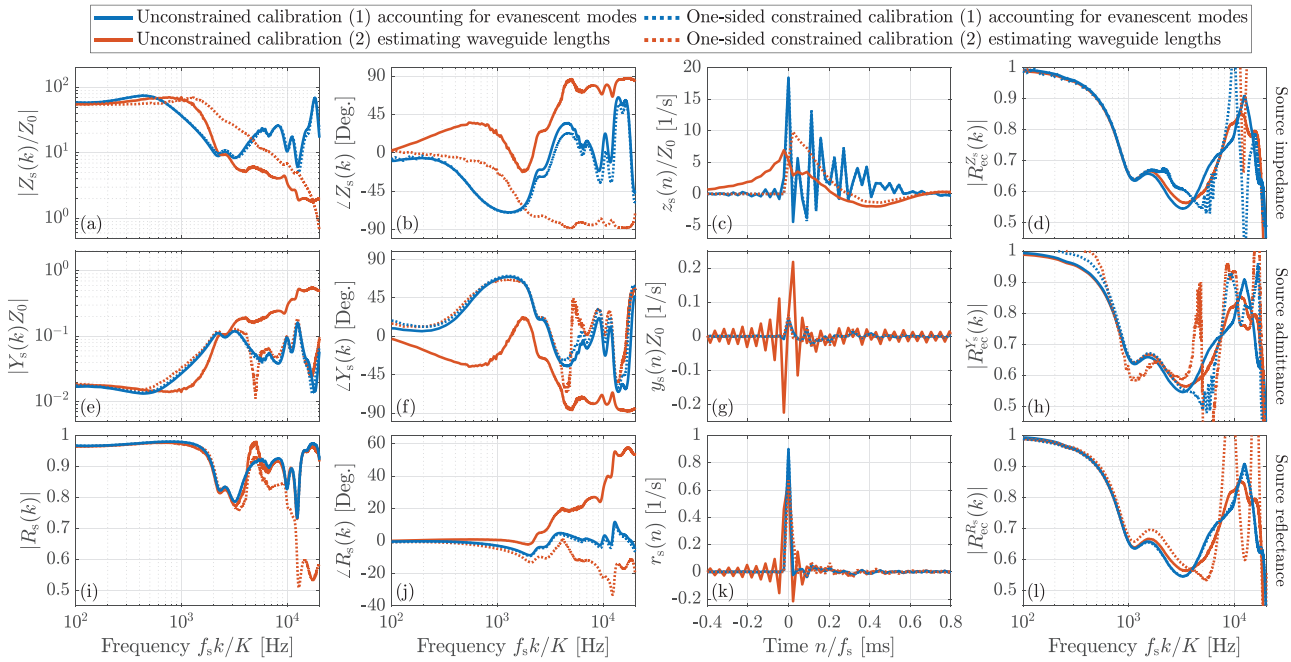

FIG. 4. (Color online) Results for unconstrained and one-sided constrained [Eqs. (15) and (17)] ear-probe calibrations using calibration (1) accounting for evanescent modes and calibration (2) acoustically estimating the calibration-waveguide lengths, based on the ear-probe transfer functions, the source [(a)–(d)] impedance $Z_s(k)$, [(e)–(h)] admittance $Y_s(k)$, and [(i)–(l)] reflectance $R_s(k)$. The [(a), (e), (i)] magnitude and [(b), (f), (j)] phase of the ear-probe transfer functions $Z_s(k)$, $Y_s(k)$, and $R_s(k)$, [(c), (g), (k)] their corresponding IDFT impulse responses $z_s(n)$, $y_s(n)$, and $r_s(n)$, and [(d), (h), (l)] the reflectance magnitudes $|R_{ec}^{Z_s}(k)|$, $|R_{ec}^{Y_s}(k)|$, and $|R_{ec}^{R_s}(k)|$ measured in the occluded-ear simulator based on the specified ear-probe transfer function. Note that impedance and admittance variables are normalized by the ear-simulator characteristic impedance Z_0.

the causal unstable non-physical negative parallel compliance would be a one-sided growing negative exponential [see Eq. (24)]. The remaining negative-time behavior in $z_s(n)$ for the unconstrained calibration (1) may be partially due to fractional sample delays, frequency windowing, and the approximate least-squares solution. Resultingly, $Z_s(k)$ and $z_s(k)$ of the one-sided constrained calibration (1) deviate only marginally from those of the unconstrained calibration (1) in Figs. 4(a)–4(c), yet $R_{ec}^{Z_s}(k)$ based on the unconstrained and one-sided constrained calibration (1) in Fig. 4(d) still deviates substantially, especially toward higher frequencies. Conversely, $Z_s(k)$ and $z_s(k)$ of the unconstrained and one-sided constrained calibration (2) in Figs. 4(a)–4(c) deviate substantially due to the time reversal of the negative-time exponential decay in $z_s(n)$, and the partly complex conjugation of $Z_s(k)$ [see Eq. (27)] is evident from Fig. 4(b). Note that most of $|R_{ec}^{Z_s}(k)|$ in Fig. 4(d) lies beyond unity for the one-sided constrained calibration (2).

For the results based on the source admittance $Y_s(k)$ in Figs. 4(e)–4(h), $Y_s(k)$ and $y_s(n)$ for the unconstrained and one-sided constrained calibration (1) in Figs. 4(e)–4(g) are again similar, yet substantial deviations between corresponding $R_{ec}^{Y_s}(k)$ can be observed in Fig. 4(h). For the unconstrained calibration (2), the negative parallel compliance C is clearly visible in Figs. 4(e) and 4(f), but its admittance $j\omega C$ now acts as an imaginary frequency-linear superposition to $Y_s(k)$, which superimposes as an odd function onto $y_s(k)$ in Fig. 4(g). Therefore, the compliance vanishes in $Y_s(k)$ and $y_s(n)$ in Figs. 4(e)–4(g) of the one-sided constrained calibration (2) [see Eqs. (15) and (17)], which are now similar to those of the unconstrained and one-sided constrained calibration (1), although still resulting in errors in $R_{ec}^{Y_s}(k)$ for the one-sided constrained calibration (2) in Fig. 4(h).

Finally, for the results based on the source reflectance $R_s(k)$ in Figs. 4(i)–4(l), despite the fact that $|R_s(k)|$ are similar for the unconstrained calibrations (1) and (2) in Fig. 4(i), the negative parallel compliance results in a negative delay in $R_s(k)$ for the unconstrained calibration (2), evident from the positive slope in $\angle R_s(k)$ in Fig. 4(j), because the source impedance $Z_s(k)$ and the impedance of the negative compliance $1/(j\omega C)$ are much larger than Z_0. $r_s(n)$ is now dominated by a negative factional sample delay for the unconstrained calibration (2) in Fig. 4(k), which introduces corresponding errors into $R_s(k)$, $r_s(n)$, and $R_{ec}^{R_s}(k)$ in Figs. 4(i) and 4(j), 4(k), and 4(l), respectively, for the constrained calibration (2). Conversely, $R_s(k)$ and $r_n(k)$ in Figs. 4(i)–4(k) are close to minimum-phase and almost identical for the unconstrained and one-sided constrained calibration (1) to such a degree that no qualitative difference can be observed between $R_{ec}^{R_s}(k)$ in Fig. 4(l).

V. DISCUSSION AND CONCLUSIONS

Physical systems are causal; thus, time impulse responses characterizing them must be one-sided. However, IDFT impulse responses synthesized from numerical transfer functions are two-sided, except for ideal cases of integer

sample delays, because they are subject to the two-sided properties of the IDFT. Thus, one-sidedness of an IDFT impulse response characterizing a physical system is neither a crucial nor an expected property. Primary sources of negative-time components in ear-canal and ear-probe IDFT impulse responses include frequency windowing and the appearance of right-hand-plane poles in the ear-probe transfer function (see below). Disregarding measurement noise and spontaneous otoacoustic emissions, these considerations apply to ears and ear probes as well as any other physical system.

The Fourier and one-sided Laplace transforms differ in their ability to handle two-sided and unbounded impulse responses, but only the forward and IDFTs can be evaluated numerically. Calculating an ILT impulse response requires a complex-analytic transfer function, e.g., estimated from the complex numerical data (Robinson *et al.*, 2013). Despite the inability of the IDFT to produce one-sided IDFT impulse responses, such transformation can be useful for a number of practical applications, e.g., estimating the ear-canal characteristic impedance and area-distance function (Rasetshwane and Neely, 2011), compensating for evanescent modes (Nørgaard *et al.*, 2017a) and oblique ear-probe insertions (Nørgaard *et al.*, 2019c), or clinical applications (Merchant *et al.*, 2019). For all these applications, minimizing the effects of frequency windowing on the IDFT impulse response is essential.

In ideal cases, a one-sided IDFT impulse response can be exactly reconstructed from its even [Eq. (15)] or odd [Eq. (16)] parts. For practical two-sided IDFT impulse responses—e.g., due to the influence of windowing and instability on the Fourier transform—negative-time components are not removed, but rather mirrored into positive time. Consequently, constraining a two-sided IDFT impulse response to be one-sided requires altering the frequency content of the corresponding transfer function. These considerations apply to acoustic transfer functions characterizing ear canals, the middle ear, and ear probes, which are inherently different from integer sample delays. Moreover, because the speed of sound is a function of frequency (Kirchhoff, 1868; Mason, 1928; Allen, 2020), integer sample delays cannot exist in any acoustic system. In particular, the ear-probe source parameters may be subject to both two-sided windowing and unstable poles when evanescent modes are not properly accounted for during the calibration procedure (Nørgaard *et al.*, 2018; Siegel *et al.*, 2018). Consequently, constraining IDFT impulse responses of transfer functions characterizing ear probes or ear canals to be one-sided introduces errors into those transfer functions because the IDFT impulse response of the true transfer function is two-sided. In some special cases where measurement errors are caused by physical phenomena that exhibit superimposed odd IDFT impulse responses, e.g., evanescent modes, the measurement errors may be remedied through the one-sided constraint. However, one might as well subtract the approximate behavior directly from the measured transfer function, as proposed by Nørgaard *et al.* (2017a).

Non-physical unstable components occur as a result of imposing inaccurate or non-physical assumptions onto a physical system and result in two-sided IDFT impulse responses. In conical horns, they occur due to the non-physical nature of the anechoic contracting horn; however, all physical horns of finite length have stable time impulse responses (Agulló *et al.*, 1995). In ear-probe source parameters, unstable components are a result of inadequately accounting for evanescent modes during the calibration procedure. In this case, the two-sided impulse response is useful for revealing the presence of the negative parallel compliance in the source impedance (Nørgaard *et al.*, 2018). When evanescent modes are accurately accounted for, the negative parallel compliance vanishes from the source parameters along with the majority of the negative-time behavior (Nørgaard *et al.*, 2018; Siegel *et al.*, 2018), an observation that we have also confirmed in this paper.

It is possible to increase the temporal resolution and mitigate some sources of two-sided IDFT impulse responses by increasing the sampling rate of the measurement system; however, there are caveats to this approach. Higher-order modes are a causal physical phenomenon (Keefe, 2020), but their low-frequency approximation as an inertance leads to a two-sided odd IDFT impulse response (Nørgaard *et al.*, 2018). Thus, increasing the bandwidth to include the propagating higher-order modes can lead to a one-sided IDFT impulse response; however, this may have detrimental implications for interpreting the ear-canal-reflectance IDFT impulse response, which is based on the assumption of one-dimensional wave propagation.

Unlike impedance and admittance impulse responses that are one-sided $h(t<0)=0$, reflectance time impulse responses are strictly one-sided $h(t\leq 0)=0$ and only include the response to a perturbing impulse and not the impulse itself. Due to the finite speed of sound, reflectance only has a purely conceptual time impulse response that cannot physically exist, and its measurement requires a subsequent deconvolution operation that removes the perturbing impulse.

We conclude that IDFT impulse responses of acoustical systems are inherently two-sided and that one-sidedness is neither a crucial nor an expected property of ear-probe or ear-canal IDFT impulse responses. However, a two-sided IDFT impulse response may reveal problematic non-physical unstable components in the transfer function, and, with the properties of the Fourier transform in mind, IDFT impulse responses may serve a number of practical or diagnostic purposes. While a two-sided time impulse response cannot provide an exact characterization of any physical system, we find the reverse argument to be logically flawed; one-sidedness, as a property of any impulse response, does not enable inferring conclusions regarding its accuracy in characterizing a specific physical system. More specifically, a one-sided IDFT impulse response cannot exactly characterize any acoustical system. Measurement accuracy must be evaluated in realistic settings by comparison with a known reference, e.g., an occluded-ear simulator for ear-

canal reflectance. To avoid the issues of two-sided IDFT impulse responses, methods suitable for measuring aural acoustic impulse responses should be restricted to the time domain (Keefe, 2020). In such a case, one-sidedness is a logical constraint to apply to ear-probe time impulse responses and an expected property of aural time impulse responses.

ACKNOWLEDGMENTS

We thank the Editor and the two anonymous reviewers for many helpful comments on the manuscript.

Agulló, J., Barjau, A., and Martínez, J. (**1988**). "Alternatives to the impulse response $h(t)$ to describe the acoustical behavior of conical ducts," J. Acoust. Soc. Am. **84**, 1606–1612.
Agulló, J., Barjau, A., and Martínez, J. (**1992**). "On the time-domain description of conical bores," J. Acoust. Soc. Am. **91**, 1099–1105.
Agulló, J., Cardona, S., and Keefe, D. H. (**1995**). "Time-domain deconvolution to measure reflection functions for discontinuities in waveguides," J. Acoust. Soc. Am. **97**, 1950–1957.
Allen, J. B. (**1986**). "Measurement of eardrum acoustic impedance," in *Peripheral Auditory Mechanisms*, edited by J. Allen, J. Hall, A. Hubbard, S. Neely, and A. Tubis (Springer-Verlag, New York), pp. 44–51.
Allen, J. B. (**2020**). *An Invitation to Mathematical Physics and Its History* (Springer Nature Switzerland AG, Cham, Switzerland).
Benade, A. H. (**1988**). "Equivalent circuits for conical waveguides," J. Acoust. Soc. Am. **83**, 1764–1769.
Chapman, D. M. F. (**1989**). "The focusing and reflection of a converging spherical wave," J. Sound Vib. **133**, 497–501.
Charaziak, K. K., and Shera, C. A. (**2017**). "Compensating for ear-canal acoustics when measuring otoacoustic emissions," J. Acoust. Soc. Am. **141**, 515–531.
Gilbert, J., Kergomard, J., and Polack, J. D. (**1990**). "On the reflection functions associated with discontinuities in conical bores," J. Acoust. Soc. Am. **87**, 1773–1780.
Gold, B., Oppenheim, A. V., and Rader, C. M. (**1969**). "Theory and implementation of the discrete Hilbert transform," in *Papers on Digital Signal Processing* (MIT, Cambridge, MA), pp. 14–42.
IEC 60318-4 (**2010**). "Occluded-ear simulator for the measurement of earphones coupled to the ear by means of ear inserts" (International Electrotechnical Commission, Geneva, Switzerland).
Karal, F. C. (**1953**). "The analogous acoustical impedance for discontinuities and constrictions of circular cross section," J. Acoust. Soc. Am. **25**, 233–237.
Keefe, D. H. (**1997**). "Otoreflectance of the cochlea and middle ear," J. Acoust. Soc. Am. **102**, 2849–2859.
Keefe, D. H. (**2020**). "Causality-constrained measurements of aural acoustic reflectance and reflection functions," J. Acoust. Soc. Am. **147**, 300–324.
Keefe, D. H., and Benade, A. H. (**1981**). "Impedance measurement source and microphone proximity effects," J. Acoust. Soc. Am. **69**, 1489–1495.
Keefe, D. H., Folsom, R. C., Gorga, M. P., Vohr, B. R., Bulen, J. C., and Norton, S. J. (**2000**). "Identification of neonatal hearing impairment: Ear-canal measurements of acoustic admittance and reflectance in neonates," Ear Hear. **21**, 443–461.
Keefe, D. H., Ling, R., and Bulen, J. C. (**1992**). "Method to measure acoustic impedance and reflection coefficient," J. Acoust. Soc. Am. **91**, 470–485.
Keefe, D. H., and Simmons, J. L. (**2003**). "Energy transmittance predicts conductive hearing loss in older children and adults," J. Acoust. Soc. Am. **114**, 3217–3238.
Kirchhoff, G. (**1868**). "On the influence of heat conduction in a gas on sound propagation," Ann. Phys. Chem. **134**, 177–193.
Mason, W. P. (**1928**). "The propagation characteristics of sound tubes and acoustic filter," Phys. Rev. **31**, 283–295.
Merchant, G. R., Siegel, J. H., Neely, S. T., Rosowski, J. J., and Nakajima, H. H. (**2019**). "Effect of middle-ear pathology on high-frequency ear canal reflectance measurements in the frequency and time domains," J. Assoc. Res. Otolaryngol. **20**, 529–552.
Nørgaard, K. R., Charaziak, K. K., and Shera, C. A. (**2019a**). "A comparison of ear-canal-reflectance measurement methods in an ear simulator," J. Acoust. Soc. Am. **146**, 1350–1361.
Nørgaard, K. R., Charaziak, K. K., and Shera, C. A. (**2019b**). "On the calculation of reflectance in non-uniform ear canals," J. Acoust. Soc. Am. **146**, 1464–1474.
Nørgaard, K. R., Fernandez-Grande, E., and Laugesen, S. (**2017a**). "Compensating for evanescent modes and estimating characteristic impedance in waveguide acoustic impedance measurements," J. Acoust. Soc. Am. **142**, 3497–3509.
Nørgaard, K. R., Fernandez-Grande, E., and Laugesen, S. (**2017b**). "Incorporating evanescent modes and flow losses into reference impedances in acoustic Thévenin calibration," J. Acoust. Soc. Am. **142**, 3013–3024.
Nørgaard, K. R., Fernandez-Grande, E., and Laugesen, S. (**2019c**). "Compensating for oblique ear-probe insertions in ear-canal reflectance measurements," J. Acoust. Soc. Am. **145**, 3499–3509.
Nørgaard, K. R., Neely, S. T., and Rasetshwane, D. M. (**2018**). "Quantifying undesired parallel components in Thévenin-equivalent acoustic source parameters," J. Acoust. Soc. Am. **143**, 1491–1503.
Oppenheim, A. V., and Schafer, R. W. (**1989**). *Discrete-Time Signal Processing* (Prentice-Hall, Englewood Cliffs, NJ).
Papoulis, A. (**1962**). *The Fourier Integral and Its Applications* (McGraw-Hill, New York).
Piskorski, P., Keefe, D. H., Simmons, J. L., and Gorga, M. P. (**1999**). "Prediction of conductive hearing loss based on acoustic ear-canal response using a multivariate clinical decision theory," J. Acoust. Soc. Am. **105**, 1749–1764.
Rasetshwane, D. M., and Neely, S. T. (**2011**). "Inverse solution of ear-canal area function from reflectance," J. Acoust. Soc. Am. **130**, 3873–3881.
Robinson, S. R., Nguyen, C. T., and Allen, J. B. (**2013**). "Characterizing the ear canal acoustic reflectance and impedance by pole-zero fitting," Hear. Res. **301**, 168–182.
Scheperle, R. A., Neely, S. T., Kopun, J. G., and Gorga, M. P. (**2008**). "Influence of *in situ*, sound-level calibration on distortion-product otoacoustic emission variability," J. Acoust. Soc. Am. **124**, 288–300.
Siegel, J. H., Nørgaard, K. R., and Neely, S. T. (**2018**). "Evanescent waves in simulated ear canals: Experimental demonstration and method for compensation," J. Acoust. Soc. Am. **144**, 2135–2146.
Souza, N. N., Dhar, S., Neely, S. T., and Siegel, J. H. (**2014**). "Comparison of nine methods to estimate ear-canal stimulus levels," J. Acoust. Soc. Am. **136**, 1768–1787.
Voss, S. E., and Allen, J. B. (**1994**). "Measurement of acoustic impedance and reflectance in the human ear canal," J. Acoust. Soc. Am. **95**, 372–384.